

RESEARCH

Open Access



Large-scale CRISPRi screens link metabolic stress to glioblastoma chemoresistance

Xing Li^{1,2†}, Wansong Zhang^{1,2†}, Yitong Fang^{1,2}, Tianhu Sun^{1,2}, Jian Chen³ and Ruilin Tian^{1,2*} 

Abstract

Background Glioblastoma (GBM) patients frequently develop resistance to temozolomide (TMZ), the standard chemotherapy. While targeting cancer metabolism shows promise, the relationship between metabolic perturbation and drug resistance remains poorly understood.

Methods We performed high-throughput CRISPR interference screens in GBM cells to identify genes modulating TMZ sensitivity. Findings were validated using multiple GBM cell lines, patient-derived glioma stem cells, and clinical data. Molecular mechanisms were investigated through transcriptome analysis, metabolic profiling, and functional assays.

Results We identified phosphoglycerate kinase 1 (*PGK1*) as a key determinant of TMZ sensitivity. Paradoxically, while *PGK1* inhibition suppressed tumor growth, it enhanced TMZ resistance by inducing metabolic stress. This activated AMPK and HIF-1 α pathways, leading to enhanced DNA damage repair through 53BP1. *PGK1* expression levels correlated with TMZ sensitivity across multiple GBM models and patient samples.

Conclusions Our study reveals an unexpected link between metabolic stress and chemoresistance, demonstrating how metabolic adaptation can promote therapeutic resistance. These findings caution against single-agent metabolic targeting and suggest *PGK1* as a potential biomarker for TMZ response in GBM.

Keywords Glioblastoma, Temozolomide resistance, *PGK1*, Metabolic stress, CRISPR screening, DNA damage repair

Background

Glioblastoma (GBM) is the most aggressive primary brain tumor, with a median survival of only 12–15 months despite aggressive treatment [1–3]. The current standard of care includes surgical resection followed by concurrent chemoradiation with temozolomide (TMZ) [4]. However, most patients eventually develop resistance to TMZ, leading to tumor recurrence and poor survival outcomes [5, 6].

Cancer cells exhibit altered metabolism, characterized by increased glycolysis even in the presence of oxygen, known as the Warburg effect [7, 8]. This metabolic reprogramming is essential for meeting the high energy demands of rapidly proliferating tumor cells and supporting various aspects of cancer progression [9, 10].

[†]Xing Li and Wansong Zhang contributed equally to this work.

*Correspondence:

Ruilin Tian

tianrl@sustech.edu.cn

¹School of Medicine, Southern University of Science and Technology, Shenzhen 518055, Guangdong Province, China

²Key University Laboratory of Metabolism and Health of Guangdong, Southern University of Science and Technology, Shenzhen 518055, Guangdong Province, China

³Research Unit of Medical Neurobiology, Chinese Institute for Brain Research, Beijing, Chinese Academy of Medical Sciences, Beijing, China



© The Author(s) 2025. **Open Access** This article is licensed under a Creative Commons Attribution-NonCommercial-NoDerivatives 4.0 International License, which permits any non-commercial use, sharing, distribution and reproduction in any medium or format, as long as you give appropriate credit to the original author(s) and the source, provide a link to the Creative Commons licence, and indicate if you modified the licensed material. You do not have permission under this licence to share adapted material derived from this article or parts of it. The images or other third party material in this article are included in the article's Creative Commons licence, unless indicated otherwise in a credit line to the material. If material is not included in the article's Creative Commons licence and your intended use is not permitted by statutory regulation or exceeds the permitted use, you will need to obtain permission directly from the copyright holder. To view a copy of this licence, visit <http://creativecommons.org/licenses/by-nc-nd/4.0/>.

Consequently, targeting cancer metabolism has emerged as a promising therapeutic strategy, with numerous studies demonstrating the effectiveness of inhibiting key metabolic enzymes in suppressing tumor growth [11–13].

However, mounting evidence suggests a complex relationship between metabolic perturbation and drug resistance [14]. While metabolic inhibition can effectively suppress tumor growth, the resulting metabolic stress may paradoxically activate cellular adaptive responses that promote survival under therapeutic pressure [15]. These stress responses, including the activation of energy sensors and survival pathways, might contribute to drug resistance [16, 17]. Nevertheless, the molecular mechanisms linking metabolic stress to drug resistance remain poorly understood, particularly in the context of GBM treatment.

In this study, we employed large-scale CRISPRi screens to systematically investigate the mechanisms underlying TMZ resistance in GBM. Our findings reveal an unexpected role of glycolytic inhibition in promoting TMZ resistance and elucidate the underlying molecular mechanisms, providing new insights into the complex interplay between cellular metabolism and drug resistance in cancer treatment.

Materials and methods

Cell culture

U87 MG, U118 MG, U251 MG, U251 MG/TMZ and HEK293T cell lines were obtained from ATCC and maintained in Dulbecco's Modified Eagle's Medium (DMEM; Gibco, Cat. no. C11995500BT) supplemented with 10% fetal bovine serum (TransGen Biotech, Cat. no. FS301-02) and 1% penicillin-streptomycin solution (Aladdin, Cat. no. P301861-100 ml). Cells were cultured under standard conditions of 37 °C in a humidified incubator with 5% CO₂. Mycoplasma contamination was ruled out using the MycAway™ Plus-Color One-Step Mycoplasma Detection Kit (Yeasen, Cat. no. 40612ES25).

Lentivirus production

For large-scale lentivirus production of the H1 library, 5 × 10⁶ HEK293T cells were seeded in 15-cm dishes and incubated for 24 h. Transfection was performed with 15 µg of the H1 library plasmid and 15 µg of third-generation packaging mix (1:1:1 ratio of the three plasmids), diluted in 3 mL Opti-MEM (Gibco, Cat. no. 31986-07). Polyethylenimine Linear (PEI, MW 40000; Yeasen, Cat. no. 40816ES03) at a final volume of 120 µL was added to the DNA solution, vortexed briefly, and incubated at room temperature for 10–15 min before being added to the cells. Viral supernatants were collected 48 h post-transfection and filtered through 0.45 µm filters (Millipore, Cat. no. SLHV033RB).

For small-scale lentivirus production, 0.5 × 10⁶ HEK293T cells were plated in 6-well plates. After 24 h, 1 µg of transfer plasmid and 1 µg of packaging mix were diluted in 100 µL Opti-MEM per well, mixed, and combined with 4 µL PEI. The mixture was briefly vortexed and added to the cells. The remaining steps were performed as described for large-scale production.

Generation of CRISPRi-U87 cell line

To generate the CRISPRi-U87 cell line, U87 MG cells were co-transfected with plasmids encoding pC13N-dCas9-BFP-KRAB [18] and TALENs targeting the CLYBL intragenic safe harbor locus (pZT-C13-R1 and pZT-C13-L1; Addgene #62196 and #62197) using Lipofectamine 3000 (Thermo Fisher Scientific, Cat. no. L3000001). Cells expressing blue fluorescent protein (BFP) were enriched via fluorescence-activated cell sorting (FACS) using a FACSaria SORP system (BD Biosciences), resulting in the CRISPRi-U87 cell line.

CRISPRi screening

The H1 library, consisting of 13,025 unique sgRNAs targeting 2,318 kinases, phosphatases and drug targets (5 or 10 sgRNAs each gene), and 500 non-targeting controls, was packaged into lentivirus and transduced into CRISPRi-U87 cells at a low multiplicity of infection (MOI) of 0.3. Transduced cells were selected with 2 µg/mL puromycin for 48 h to eliminate uninfected cells and establish a genome-edited cell pool. Cells were harvested, and genomic DNA was extracted using DNAiso Reagent (Takara, Cat. no. 9770Q). sgRNA regions were amplified with 2× Phanta Flash Master Mix (Vazyme, Cat. no. P510-02) and purified using Hieff NGS DNA Selection Beads (Yeasen, Cat. no. 12601ES08). The sgRNA libraries were sequenced on a DNBSEQ-T7 platform (MGI Tech). The MAGeCK-iNC pipeline was used for screening data analysis [18–20].

sgRNA cloning

Individual sgRNAs were cloned into the pLG15 vector through BstXI and Bpu1102I restriction sites following previously established protocols [21]. The pLG15 vector includes a mouse U6 promoter for sgRNA expression, along with an EF-1α promoter driving puromycin resistance and BFP expression for selection. The sgRNA sequences used in this study are detailed in Supplementary Table 3.

Cell cycle analysis

Cell cycle distribution was analyzed after trypsinizing the cells and fixing them in 70% ethanol. Fixed cells were stained using a propidium iodide solution from the Cell Cycle and Apoptosis Analysis Kit (Yeasen, Cat. no. 40302ES60). DNA content was assessed via flow

cytometry using a FACSCanto SORP instrument (BD Biosciences).

Cell counting via flow cytometry

Cells were harvested and counted using a flow cytometer (Agilent, NovoCyte) to quantify cell numbers under different treatment conditions. Following treatment, cells were trypsinized to achieve a single-cell suspension and resuspended in an equal volume of DPBS medium. To ensure consistency, the suspension was gently pipetted multiple times to prevent clumping and ensure homogeneity. A fixed volume of the cell suspension was loaded into the flow cytometer for analysis. Cell counts were recorded based on fluorescence intensity or forward/side scatter gating, ensuring only live and single cells were included in the final count. Results were averaged across three replicates for each condition to ensure statistical reliability.

Western blot analysis

Total protein lysates were prepared by lysing U87 MG cells in RIPA buffer (Beyotime, Cat. no. P0013B), and protein concentration was quantified with a bicinchoninic acid (BCA) protein assay kit (TransGen Biotech, Cat. no. DQ111-01). Equal amounts of protein were resolved by SDS-PAGE, followed by transfer to polyvinylidene difluoride (PVDF) membranes (Beyotime, Cat. no. FFP39). Membranes were blocked, probed with primary antibodies overnight, and incubated with secondary antibodies. Protein bands were visualized using an enhanced chemiluminescence detection kit (Epizyme, Cat. no. SQ201). Antibodies used included anti-HIF1 α (CST, 36169 S; 1:1000), anti-AMPK (CST, 2532 S; 1:1000), anti-p-AMPK (CST, 74281SF; 1:1000), anti-Histone 3 (CST, 4499 S; 1:2000), anti-53BP1 (Abcam, ab130275; 1:1000), anti- γ H2A.X (Abmart, T56572M; 1:1000), anti-Tubulin (Proteintech, 11224-1-AP; 1:5000), and anti-ACTB (Proteintech, 81115-1-RR; 1:5000). Quantification of protein bands was performed using ImageJ software (<http://rsb.info.nih.gov/ij/>).

Quantitative real-time polymerase chain reaction (qRT-PCR)

RNA was isolated using the MolPure[®] Cell RNA Kit (Yeasen, Cat. no. 19231ES50) and converted to cDNA with the TransScript[®] One-Step gDNA Removal and cDNA Synthesis SuperMix (TransGen, Cat. no. AT311-03). Real-time qPCR was carried out with AceQ qPCR SYBR Green Master Mix (Vazyme, Cat. no. Q111-02) on a QuantStudio 7 Flex thermocycler (Applied Biosystems). GAPDH served as an internal control. The sequences of qPCR primers are listed in Supplementary Table 3.

CCK-8 cytotoxicity assay

Cell proliferation was evaluated using the Cell Counting Kit-8 (TargetMol, Cat. no. C0005). Approximately 1,000 cells per well were seeded in 96-well plates with 200 μ L culture medium. After 24 h, 10 μ L of CCK-8 solution was added to each well, and the plates were incubated at 37 $^{\circ}$ C for 1 h. Absorbance at 450 nm was measured using a microplate reader (Agilent, SH1M), with 650 nm as the reference wavelength.

Oxygen consumption rate (OCR) and extracellular acidification rate (ECAR) measurements

OCR and ECAR were assessed using the Seahorse XF Cell Mitochondria Stress Test Kit (Agilent, Cat. no. 103015-100) and Seahorse XF Glycolysis Rate Assay Kit (Agilent, Cat. no. 103020-100), respectively, on a Seahorse XFe96 Bioenergetic Analyzer (Agilent). U87 MG cells were plated at 5×10^4 cells/well in 96-well plates and incubated overnight. For OCR, 10 mM glucose, 1 mM pyruvate and 2 mM glutamine as a substrate, cells were washed with Seahorse buffer before automated injections of oligomycin (1.5 μ M), FCCP (1 μ M), and a combination of rotenone and antimycin (0.5 μ M each). For ECAR, 2 mM glutamine as a substrate, 10 mM glucose, 1.5 μ M oligomycin, and 50 mM 2-deoxyglucose (2-DG) were sequentially added to cells. Data were normalized using Seahorse Wave Desktop software.

Cellular oxidative stress

Intracellular reactive oxygen species (ROS) levels were determined by measuring the oxidation of 2',7'-dichlorodihydrofluorescein diacetate (DCFH-DA; Beyotime, Cat. no. S0033M) to fluorescent DCFH. Cells were incubated with 10 μ M DCFH-DA in culture medium at 37 $^{\circ}$ C for 30 min. The fluorescence intensity of DCFH was analyzed by flow cytometry, and samples without DCFH-DA served as negative controls. Data were corrected by subtracting the negative control fluorescence values.

ATP measurement

Cellular ATP levels were quantified using the Enhanced ATP Assay Kit (Beyotime, Cat. no. S0026). The assay buffer was mixed with the substrate at room temperature to prepare the reagent. Each sample was incubated with 100 μ L of reagent for 15 min at room temperature, and luminescence was measured using a microplate reader. ATP levels were expressed as a percentage relative to the control.

Immunofluorescence

Cells were cultured on glass slides and subjected to various treatments before being fixed in pre-cooled methanol for 20 min. After three PBS washes, cells were incubated overnight at 4 $^{\circ}$ C with anti- γ H2A.X antibodies (Abmart,

Cat. no. T56572M) in a solution containing 0.1% Triton X-100 and 1% BSA. Secondary antibodies and DAPI were subsequently applied at room temperature for 2 h. Fluorescent images were acquired using a Nikon A1R fluorescence microscope.

Luciferase reporter assay

The Dual-Luciferase Reporter Assay System (Promega, Cat. no. E1910) was used following the manufacturer's instructions. Cells were plated in 24-well plates at 4×10^4 cells per well and co-transfected with 0.5 μg of firefly luciferase reporter plasmid (pGL3 or Hind III-digested pGL3) and 0.05 μg of Renilla luciferase control plasmid (pRL-SV40). After 48 h, luciferase activities were measured, and firefly luciferase activity was normalized to Renilla luciferase activity.

RNA sequencing and data analysis

Total RNA was extracted using the Total RNA Extraction Reagent (Invitrogen, Cat. no. 15596018) according to the manufacturer's protocol. cDNA libraries for RNA sequencing were prepared using the Hieff NGS[®] Ultima Dual-mode RNA Library Prep Kit for Illumina[®] (Yeasten, Cat. no. 12252ES08). Sequencing was performed on the DNBSEQ-T7 platform (GenePlus, Shenzhen, China) with at least 12 Gb of PE150 sequencing data per sample.

The RNA-seq data were mapped to the GRCh38 reference genome using STAR (v2.7.6a), and gene expression levels were quantified with StringTie2 (v2.0.4). Expression levels were normalized using Fragments Per Kilobase of transcript per Million mapped reads (FPKM) and the results have been presented in the Supplementary Table 4. Differential expression analysis was conducted using DESeq2 (v1.26.0), with significance defined as an adjusted P value ($p \text{ adj}$) ≤ 0.05 and fold change ≥ 2 (\log_2 (fold change) > 1).

KEGG enrichment analysis were performed to deduce the potential biological functions by an R package-clusterProfiler (version 3.14.0). Genes with at least one read in treatment or control samples were considered the enrichment analysis background.

Public data mining

The Cancer Treatment Response Gene Signature Database (CTR-DB) is a comprehensive resource that contains patient-derived gene expression signatures meticulously correlated with detailed cancer drug response data. (http://ctrdb.cloudna.cn/analysisResult?level=browse%26dataType=%26id=CTR_RNAseq_38-I, http://ctrdb.cloudna.cn/analysisResult?level=browse%26dataType=%26id=CTR_RNAseq_342-I, [CTR_RNAseq_20-I](http://ctrdb.cloudna.cn/analysisResult?level=browse%26dataType=%26id=CTR_RNAseq_20-I)).

Statistical analysis

Statistical comparisons were carried out using GraphPad Prism 9. The Student's t -test was applied for pairwise group comparisons, while one-way ANOVA was used for experiments involving 3 or more groups. Data are presented as mean \pm Standard deviation (SD). P values of less than 0.05 were considered statistically significant (* < 0.05 , ** < 0.01 and *** < 0.001).

Results

Pooled CRISPRi screens identified genetic vulnerabilities underlying TMZ resistance of GBM cells

To systematically investigate the mechanisms underlying glioblastoma chemoresistance, we conducted large-scale CRISPR interference (CRISPRi) screens. For this purpose, we first engineered a U87 MG cell line that stably expresses the CRISPRi machinery, referred to as CRISPRi-U87, by integrating a CAG promoter-driven dCas9-BFP-KRAB expression cassette into the CLYBL safe harbor locus via homologous recombination [22]. Robust gene silencing efficiency in CRISPRi-U87 cells was validated using three previously characterized sgRNAs targeting *STAT1*, *TFRC*, and *IFNAR* [18, 22].

To determine an optimal temozolomide (TMZ) concentration for the screen, we assessed the sensitivity of CRISPRi-U87 cells to TMZ using the CCK-8 assay (Supplementary Fig. 1A&B). The half-maximal inhibitory concentration (IC₅₀) was determined to be 50.71 μM . For the screen, we chose a TMZ concentration of 50 μM , close to the IC₅₀, to enable the identification of genes regulating TMZ sensitivity in both directions (i.e., genes whose knockdown either increases or decreases sensitivity).

We utilized the H1 library for the screen, which contains approximately 13,000 sgRNAs targeting 2,318 genes, including kinases, phosphatases, and drug targets, with 5–10 sgRNAs per gene and 500 non-targeting control sgRNAs [21]. The screen comprised two arms: a growth screen, aimed at identifying genes required for glioblastoma growth under normal conditions, and a TMZ sensitivity screen, designed to uncover genes influencing glioblastoma susceptibility to TMZ. CRISPRi-U87 cells were transduced with the sgRNA library, and after selection, split into two groups: one treated with 50 μM TMZ, and the other treated with DMSO (Vehicle). Each condition was performed in duplicate. Genomic DNA was extracted from cells at the start of treatment (D0) and after 7 days (D7) and 14 days (D14). The sgRNA-containing regions were PCR-amplified and sequenced via next-generation sequencing (NGS). We used the MAGeCK pipeline to quantify sgRNA abundances and infer gene knockdown phenotypes (Fig. 1A).

In the growth screen, sgRNA abundances from D7 and D14 samples in the Vehicle group were compared to

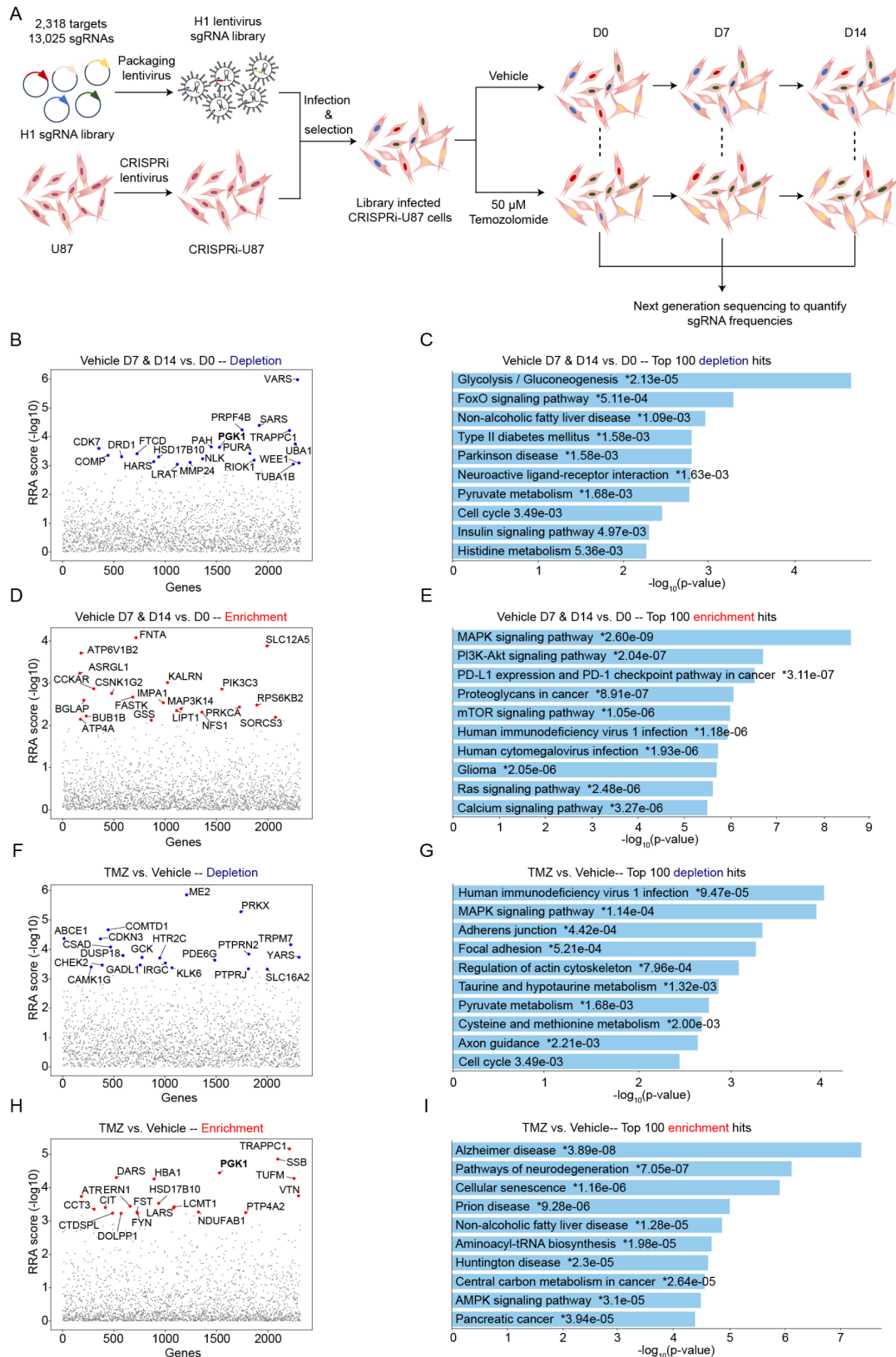


Fig. 1 (See legend on next page.)

(See figure on previous page.)

Fig. 1 Large-scale CRISPRi screens identifies genetic determinants of TMZ resistance in U87 cells. **A.** Schematic workflow of the large-scale CRISPRi screen. U87 cells stably expressing dCas9-KRAB (CRISPRi-U87) were transduced with the H1 sgRNA library containing ~13,000 sgRNAs targeting 2,318 genes (5–10 sgRNAs/gene) and 500 non-targeting controls. Following puromycin selection, cells were split into two arms and treated with either 50 μ M TMZ or DMSO (Vehicle). Genomic DNA was extracted at three timepoints: before treatment (D0), and after 7 (D7) and 14 days (D14) of treatment. sgRNA frequencies were quantified by next-generation sequencing of PCR-amplified sgRNA regions. The screen was performed in biological duplicate for each condition. **B-E.** Growth screen results: RRA scores from the MAGeCK analysis showing depletion (**B**) and enrichment (**D**) phenotypes for each gene perturbation, comparing sgRNA frequencies in D7 and D14 samples against D0 samples under vehicle treatment. KEGG pathway enrichment analyses of the top 100 depletion (**C**) and enrichment (**E**) hits are shown. **F-I.** TMZ sensitivity screen results: RRA scores from the MAGeCK analysis showing depletion (**F**) and enrichment (**H**) phenotypes for each gene perturbation, comparing sgRNA frequencies in TMZ-treated samples against vehicle-treated samples. KEGG pathway enrichment analyses of the top 100 depletion (**G**) and enrichment (**I**) hits are shown

those from D0 samples. Genes with significantly enriched or depleted sgRNAs were defined as hits, corresponding to those whose knockdown promoted or suppressed glioblastoma cell growth, respectively. Pathway analysis of the top 100 depletion hits revealed significant enrichment for essential tumor growth pathways such as glycolysis, FoxO signaling, and cell cycle pathways, confirming the reliability of the screen (Fig. 1B-E).

In the TMZ sensitivity screen, sgRNA abundances in TMZ-treated groups were compared against vehicle-treated groups, revealing numerous genes whose knockdown modulated sensitivity to TMZ. These included genes whose silencing either enhanced or suppressed TMZ sensitivity of glioblastoma cells. Further pathway enrichment analysis indicated key biological pathways associated with these top hits, corresponding to genes whose knockdown either exacerbated or mitigated glioblastoma resistance to TMZ (Fig. 1F-I).

Knockdown of *PGK1* Enhanced TMZ Resistance in GBM cells

Among the identified hits, phosphoglycerate kinase 1 (*PGK1*) emerged as a particularly notable candidate, exhibiting opposing phenotypes in the two screens (Fig. 2A-C): it was strongly depleted in the growth screen (Fig. 1B), indicating its essentiality for U87 growth under normal conditions, but strongly enriched in the TMZ sensitivity screen (Fig. 1H), suggesting that its knockdown enhances glioblastoma cell resistance to TMZ. Importantly, all five sgRNAs targeting *PGK1* showed consistent phenotypes in both screens, with the effects intensifying from Day 7 to Day 14 (Fig. 2B&C), excluding the possibility that the results were due to off-target effects of any particular sgRNA. These findings suggest a dual role for *PGK1* in glioblastoma: its knockdown impairs cell growth but confers TMZ resistance.

PGK1 is a rate-limiting enzyme in the glycolytic pathway, catalyzing the conversion of 1,3-bisphosphoglycerate (1,3-BPG) and ADP into 3-phosphoglycerate (3-PG) and ATP [23]. *PGK1* is highly expressed in various types of tumors and plays multifaceted roles in promoting tumor cell growth and proliferation [24, 25] (Fig. 2D).

To validate our screen results, we individually cloned two sgRNAs targeting *PGK1* (sg*PGK1*#1 and sg*PGK1*#2) and a non-targeting control sgRNA (sgCtrl), then

transduced them into CRISPRi-U87 cells. Robust suppression of *PGK1* expression by both *PGK1*-targeting sgRNAs was confirmed by qPCR (Supplementary Fig. 2A). We assessed the effects of *PGK1* knockdown on GBM growth and TMZ resistance using three complementary approaches.

First, we monitored cell proliferation by cell counting, comparing control and *PGK1* knockdown cells treated with either 50 μ M TMZ or DMSO control (Vehicle) at multiple timepoints from Day 2 to Day 8. Under vehicle treatment, *PGK1* knockdown significantly reduced U87 cell proliferation, validating our screen results and aligning with previous reports of *PGK1*'s essential role in tumor growth (Fig. 2E). Strikingly, *PGK1* knockdown significantly enhanced TMZ resistance in U87 cells: while TMZ treatment nearly eliminated all control cells after 6 days, a substantial number of *PGK1* knockdown cells remained viable and continued to proliferate, as evidenced by increased cell counts between Day 6 and Day 8 (Fig. 2F).

Next, we performed cell cycle analyses. In control cells, TMZ treatment induced cell cycle arrest at the S + G2/M phase, consistent with its role as an alkylating agent that causes DNA damage and inhibits proliferation. Notably, *PGK1* knockdown alleviated this arrest, allowing cells to bypass TMZ-induced cell cycle arrest (Fig. 2G).

Finally, we validated our findings by a competitive growth assay. We co-cultured cells expressing a control sgRNA and a green fluorescent protein GFP with cells expressing either a control sgRNA or *PGK1*-targeting sgRNA and a blue fluorescent protein BFP at a 1:1 ratio under DMSO or varying TMZ concentrations (25 μ M, 50 μ M, and 100 μ M). Cells were collected every three days, and proportions of BFP + and GFP + cells were measured by flow cytometry to determine relative growth of the two populations (Fig. 2H). Under DMSO conditions, *PGK1* knockdown cells exhibited growth defects, as evidenced by a gradual decline in the proportion of cells expressing *PGK1* sgRNAs. However, under TMZ treatment, particularly at higher concentrations, *PGK1* knockdown cells showed significant growth advantages compared to control cells (Fig. 2I).

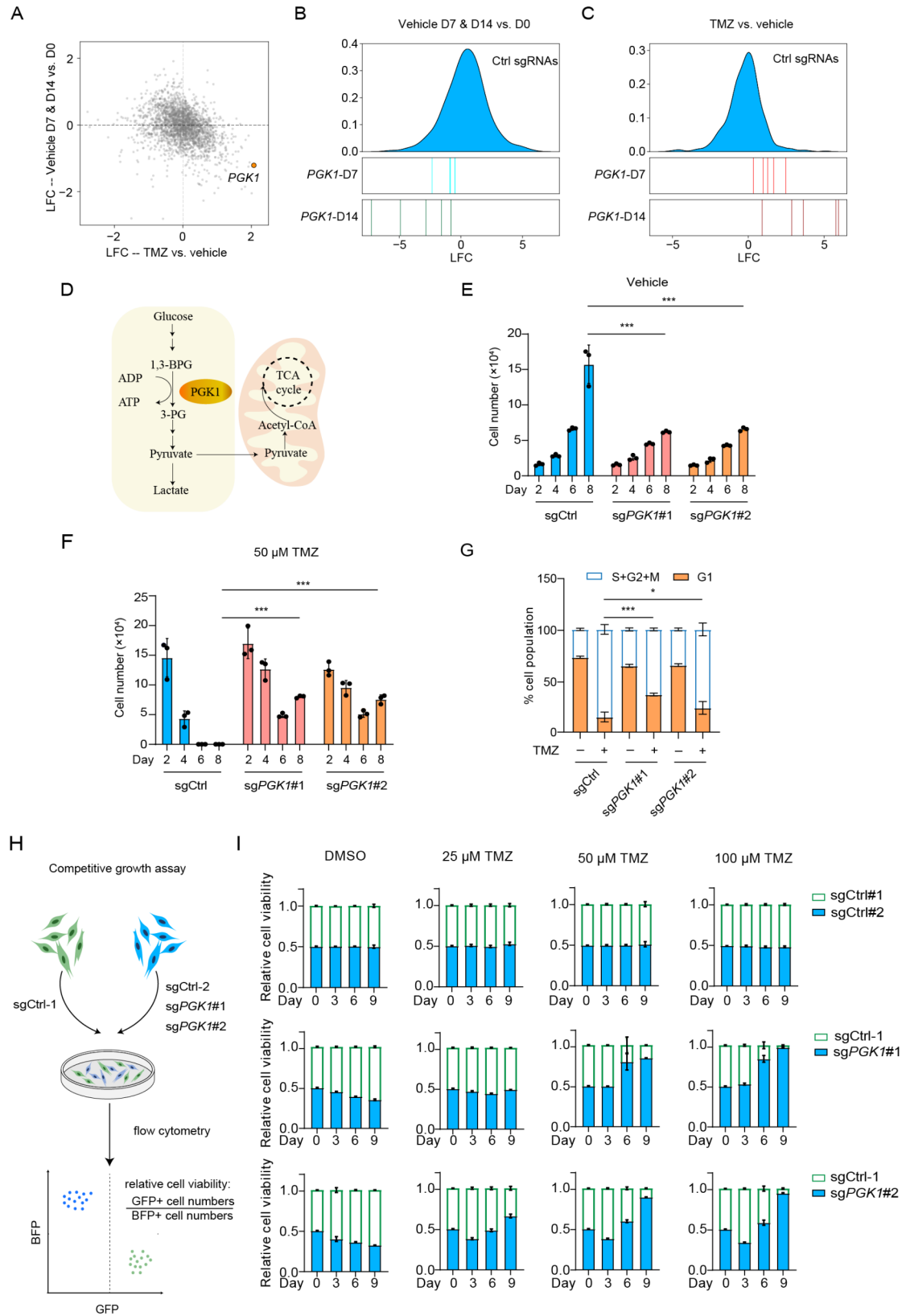


Fig. 2 (See legend on next page.)

(See figure on previous page.)

Fig. 2 *PGK1* knockdown enhances TMZ resistance despite suppressing basal growth. **A.** Comparing results from the growth screen and TMZ resistance screen, highlighting *PGK1*'s dual role in growth inhibition and TMZ resistance. **B, C.** Individual sgRNA abundance plots for 5 *PGK1*-targeting sgRNAs compared to control sgRNAs at Day 7 and Day 14 in the growth screen (**B**) and TMZ resistance screen (**C**). **D.** Schematic showing *PGK1*'s role in glycolysis pathway. **E, F.** Cell proliferation measurements comparing sgCtrl and sg*PGK1* cells treated with DMSO (**E**) or 50 μ M TMZ (**F**) over 8 days ($n=3$). Error bars denote SD. **G.** Cell cycle analysis showing distribution of cells in G1 and S+G2/M phases after 24 h TMZ treatment comparing sgCtrl and sg*PGK1* cells ($n=3$). Error bars denote SD. **H, I.** Competitive growth assay design (**H**) and results (**I**) showing relative viability of co-cultured sgCtrl and sg*PGK1* cells under varying TMZ concentrations ($n=3$). Error bars denote SD

Together, these results validate our screen findings that inhibiting *PGK1* impairs U87 growth under basal conditions but paradoxically confers TMZ resistance.

***PGK1* knockdown blocked transcriptional response to TMZ and activated pro-survival pathways in GBM cells**

To investigate the molecular mechanisms underlying TMZ resistance in *PGK1*-knockdown cells, we performed RNA-seq on CRISPRi-U87 cells expressing either sgCtrl or sg*PGK1*, treated by vehicle or 50 μ M TMZ.

Transcriptomic analysis revealed extensive gene expression changes in TMZ-treated sgCtrl cells compared to vehicle treatment, with over 4,500 upregulated and 600 downregulated differentially expressed genes (DEGs). Strikingly, significantly fewer transcriptional alterations were observed in the sg*PGK1* group under TMZ treatment, suggesting that *PGK1* knockdown suppresses the transcriptional response of U87 cells to TMZ (Fig. 3A-C, Supplementary Table 4).

Principal component analysis (PCA) further highlighted the profound transcriptomic shifts induced by TMZ in sgCtrl cells (Fig. 3D). Under TMZ treatment, sgCtrl cells formed distinct clusters separate from the vehicle-treated group when projecting gene expression profiles onto the two major components, PC1 and PC2. In contrast, *PGK1* knockdown cells treated with TMZ failed to form distinct clusters, displaying profiles that closely resembled the vehicle-treated group. This finding indicates that *PGK1* knockdown attenuates the global transcriptional reprogramming typically triggered by TMZ. Consistent with this, we identified gene sets that were significantly up- or down-regulated in control cells following TMZ treatment, but these regulations were absent in *PGK1*-knockdown cells under similar conditions (Fig. 3E).

To further explore the effects of *PGK1* knockdown, we determined DEGs by comparing sg*PGK1* groups to sgCtrl groups (Fig. 3F&H). KEGG pathway enrichment analysis showed that genes upregulated in sg*PGK1* groups were enriched in multiple pro-survival pathways, including tumor necrosis factor (TNF) signaling, NF-kappa B (NF- κ B) signaling, and phosphoinositide 3-kinase (PI3K)-Akt signaling pathways (Fig. 3G&I).

TNF-related molecules exert a variety of paradoxical effects on cancer cells, ranging from inhibitory to stimulatory. Members of the TNF family can function as tumor promoters by stimulating malignant cell proliferation,

invasion, metastasis, and angiogenesis [26, 27]. All established hallmarks of cancer are associated with NF- κ B activation. Beyond enhancing cancer cell proliferation and survival, NF- κ B also drives genetic and epigenetic alterations, cellular metabolic reprogramming, the acquisition of cancer stem cell characteristics, epithelial-to-mesenchymal transition, invasion, angiogenesis, metastasis, therapy resistance, and the suppression of antitumor immunity [28]. The PI3K/Akt signaling pathway is a critical regulator in various types of cancer. Akt-mediated downstream regulation influences numerous cellular processes, including tumor growth, cell survival, proliferation, immune responses, metabolic reprogramming, and angiogenesis. Dysregulation of the PI3K/Akt pathway also significantly contributes to drug resistance in cancers, notably in lung and esophageal cancers [29]. The activation of these survival pathways may contribute to the enhanced TMZ resistance observed in *PGK1* knockdown cells.

In summary, these results confirm that *PGK1* knockdown desensitizes U87 cells to TMZ treatment at the transcriptome level. Additionally, they demonstrate that *PGK1* knockdown activates pro-survival pathways, providing a potential explanation for the observed resistance to TMZ.

HIF-1 α pathway is activated in *PGK1* knockdown cells, contributing to TMZ resistance

Our transcriptomic analysis revealed that the expression levels of hypoxia-inducible factor 1-alpha (HIF-1 α , encoded by *HIF1A*), a transcription factor activated under hypoxic conditions, and its well-characterized downstream target *CA9*, were significantly upregulated in *PGK1* knockdown cells (Fig. 4A&B). Consistently, we confirmed elevated HIF-1 α protein levels in these cells by western blot analysis (Fig. 4C&D). These findings indicate that the HIF-1 α pathway is activated in *PGK1* knockdown cells.

To investigate whether HIF-1 α activation contributes to TMZ resistance, we cultured U87 cells under hypoxic conditions (1% O₂) to induce HIF-1 α and compared their TMZ susceptibility to that of cells cultured under normoxic conditions (21% O₂). Cell viability was assessed on days 2, 4, 6, and 8 of treatment using the CCK-8 assay (Fig. 4E-G). The results showed that while hypoxia slowed cell proliferation under vehicle treatment, it significantly enhanced cell viability under TMZ treatment

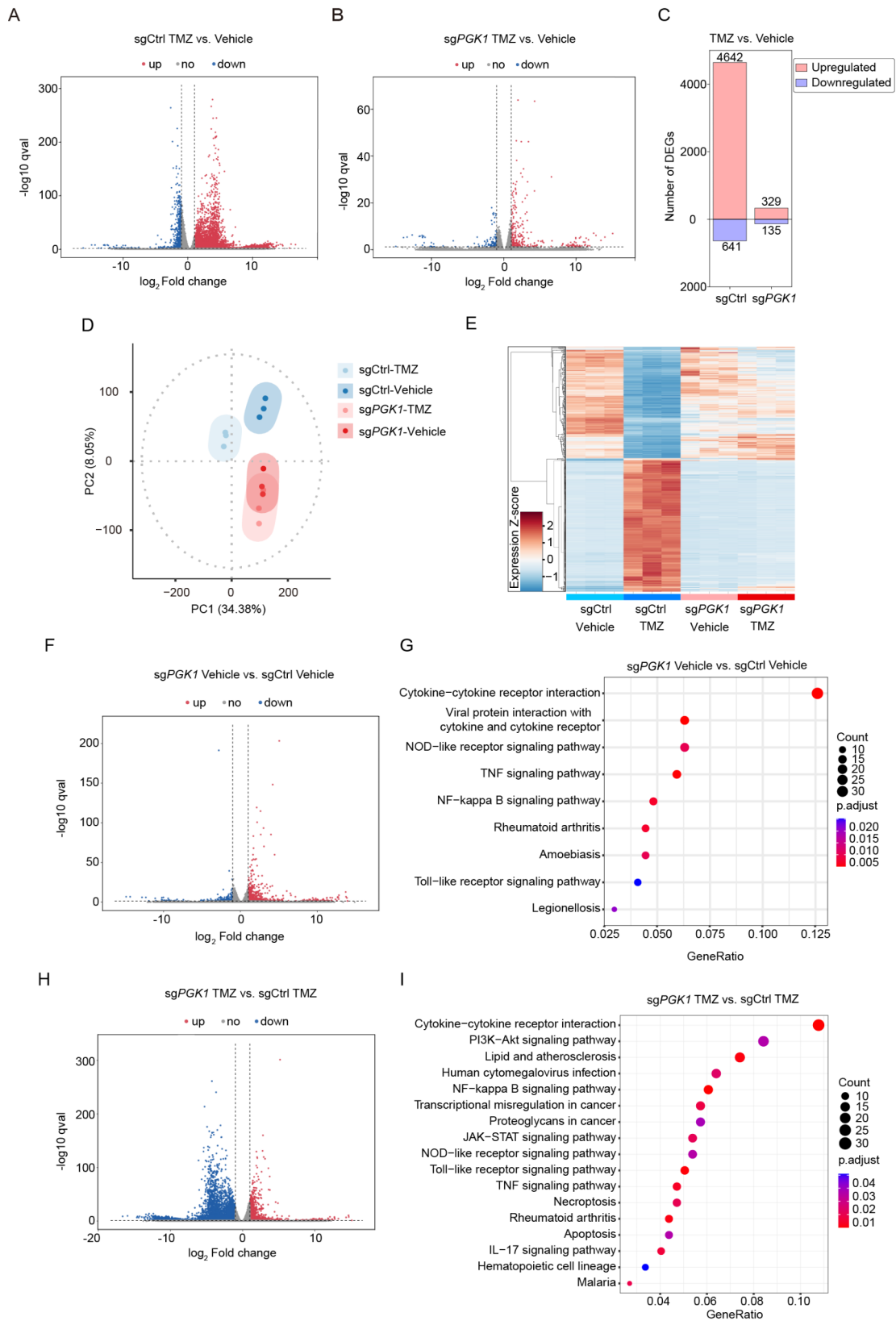


Fig. 3 (See legend on next page.)

(See figure on previous page.)

Fig. 3 Knockdown of *PGK1* blocks transcriptional response to TMZ and upregulates pro-survival pathways in U87 cells. **A-C.** Volcano plots showing differential gene expression in TMZ vs. vehicle treatment for sgCtrl (**A**) and sg*PGK1* (**B**) cells, with quantification of DEG numbers (**C**). **D.** Principal Component Analysis (PCA) of expression profiles across all conditions. **E.** Heatmap showing distinct gene expression patterns between sg*PGK1* and sgCtrl groups. **F-I.** Differential expression analysis between sg*PGK1* and sgCtrl cells in vehicle (**F, G**) and TMZ (**H, I**) conditions, with corresponding KEGG pathway enrichment analyses

across multiple time points and concentrations, mirroring the effects observed in *PGK1* knockdown cells.

To further investigate whether HIF-1 α contributes to the TMZ resistance observed in *PGK1* knockdown cells, we introduced a second sgRNA targeting *HIF1A* into cells expressing a *PGK1*-targeting sgRNA, thereby achieving dual knockdown of both *HIF1A* and *PGK1*. Competitive growth assays demonstrated that the knockdown of *HIF1A* effectively restored TMZ sensitivity in *PGK1* knockdown cells (Fig. 4H), suggesting that HIF-1 α activation plays a key role in mediating TMZ resistance in *PGK1* knockdown cells.

In addition to hypoxia, HIF-1 α can also be induced by reactive oxygen species (ROS) under normoxic conditions [30, 31]. Since *PGK1* is a rate-limiting enzyme in glycolysis, we hypothesized that its knockdown could shift cellular energy generation from glycolysis to oxidative phosphorylation, a process that generates ROS during mitochondrial electron transport. Using a Seahorse XF assay, we detected elevated maximal respiration levels in *PGK1* knockdown cells (Fig. 4I&J). Furthermore, flow cytometry analysis using a fluorescent ROS probe revealed significantly increased ROS levels in *PGK1* knockdown cells (Fig. 4K&L).

Collectively, these results demonstrate that TMZ resistance in *PGK1* knockdown cells is partially mediated by HIF-1 α pathway activation, possibly driven by elevated ROS levels.

***PGK1* knockdown leads to energy stress and AMPK activation**

Cancer cells preferentially use glycolysis for energy production, even when sufficient oxygen is available for oxidative phosphorylation, a phenomenon known as the Warburg effect [7, 32]. Therefore, knockdown of *PGK1*, a key enzyme in glycolysis, may block glycolysis and thus reduce energy production in U87 cells. In line with this hypothesis, we observed a significant reduction in glycolysis, glycolytic capacity and glycolytic reserve following *PGK1* knockdown in U87 cells using Seahorse XF analysis (Fig. 5A&B), and a significant reduction of cellular ATP levels using a bioluminescent ATP measurement assay (Fig. 5C). The shortage of energy may explain the slower proliferation observed for *PGK1* knockdown cells under basal conditions.

Energy shortage induces metabolic stress, which then activates cellular energy sensing mechanisms to restore energy homeostasis [9, 33]. AMP-activated protein

kinase (AMPK) is one of the most important energy sensors in the cell, which is phosphorylated at T172 site and activated upon changes in the ATP-to-AMP ratio under metabolic stress [34–36]. Given reduced ATP levels in *PGK1* knockdown cells, we examined whether AMPK was activated in these cells. Indeed, western blot analysis revealed significantly elevated levels of phosphorylated AMPK (T172) in *PGK1* knockdown U87 cells compared to control cells, confirming AMPK pathway activation in these cells (Fig. 5D&E).

To establish the functional significance of AMPK activation in TMZ resistance, we employed both genetic and pharmacological approaches. Genetic suppression of AMPK using a second sgRNA in *PGK1* knockdown cells restored TMZ sensitivity, as demonstrated by competitive growth assay (Fig. 5G). Pharmacological modulation of AMPK activity further supported this finding. We treated U87 cells with either AICAR (also known as acadesine), an AMPK activator, or Compound C (also known as dorsomorphin), an AMPK inhibitor. Western blot analysis confirmed the dose-dependent activation or inhibition of AMPK by these drugs (Fig. 5H). We then examined how AMPK modulation influenced TMZ sensitivity. Cell cycle analyses revealed that AICAR-induced AMPK activation in control cells conferred TMZ resistance, as indicated by reduced cell cycle arrest. In contrast, Compound C-induced AMPK inhibition in *PGK1* knockdown cells sensitized these cells to TMZ, as indicated by enhanced cell cycle arrest (Fig. 5I). These findings demonstrate that *PGK1* knockdown causes metabolic stress and activates AMPK, which plays a critical role in mediating TMZ resistance in GBM cells.

Furthermore, we observed significant activation of AMPK under hypoxic conditions, where HIF-1 α is upregulated (Fig. 5F), suggesting that AMPK activation may function downstream of HIF-1 α signaling.

***PGK1* knockdown enhances DNA Damage repair through the AMPK-53BP1 axis**

AMPK activation has been reported to promote DNA damage repair [37]. We investigated whether this mechanism contributes to the TMZ resistance observed in *PGK1* knockdown cells. To address this, we measured DNA damage levels in cells treated with TMZ using γ H2A.X staining, a widely recognized marker of DNA damage. As expected, TMZ, an alkylating agent, induced significant DNA damage in control U87 MG cells, as quantified by both imaging and western blot analysis.

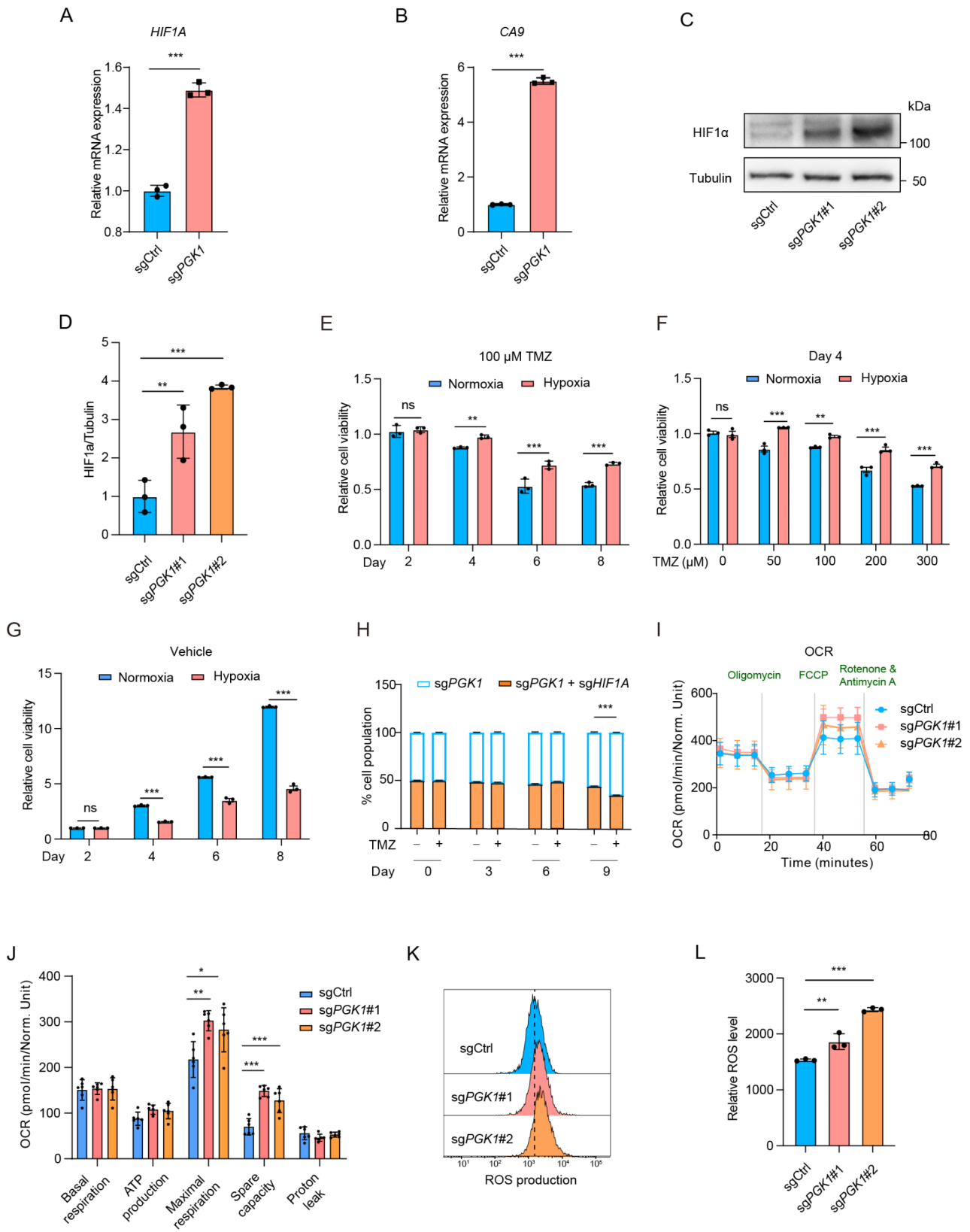


Fig. 4 (See legend on next page.)

(See figure on previous page.)

Fig. 4 HIF-1 α pathway activation contributes to TMZ resistance in *PGK1* knockdown cells. **A-D.** HIF-1 α pathway activation in *PGK1* knockdown cells shown by mRNA levels of *HIF1A* and *CA9* (**A, B**) from RNA-seq and protein levels of HIF-1 α by western blot (**C, D**). D data are presented as mean \pm SD from 3 independent experiments. **E-G.** Cell viability analysis comparing U87 cells under normoxic (21% O₂) versus hypoxic (1% O₂) conditions. (**E**) Time-course analysis of cell viability under 100 μ M TMZ treatment at days 2, 4, 6, and 8. (**F**) Cell viability after 4 days of TMZ treatment at indicated concentrations (0-300 μ M). (**G**) Cell proliferation measured by CCK-8 assay under vehicle (DMSO) treatment over 8 days. Data are presented as mean \pm SD from 3 independent experiments. **H.** Competitive growth assay showing reversal of TMZ resistance by *HIF1A* knockdown in *PGK1* knockdown cells. Data are presented as mean \pm SD from 3 independent experiments. **I-L.** Metabolic changes in *PGK1* knockdown cells showing increased mitochondrial respiration analyzed by Seahorse assay (**I, J**) ($n=6$). Error bars denote SD. Elevated ROS levels measured by flow cytometry using a fluorescent probe (**K, L**). Data are presented as mean \pm SD from 3 independent experiments

TMZ-induced DNA damage levels were comparable in *PGK1* knockdown cells (Fig. 6A&B, Supplementary Fig. 3), indicating that *PGK1* inhibition does not alter the initial DNA damage caused by TMZ.

Next, we assessed DNA damage repair efficiency by quantifying DNA damage levels after a 24 h recovery period following TMZ removal. Notably, *PGK1* knockdown cells exhibited significantly accelerated DNA damage repair compared to control cells (Fig. 6C&D).

To further validate these findings, we utilized a luciferase-based DNA damage repair assay (Fig. 6E). In this assay, a plasmid containing an SV40 promoter-driven firefly luciferase expression cassette was cleaved by the restriction enzyme Hind III, creating a DNA break between the promoter and the luciferase coding sequence. The cleaved plasmid was then transfected into cells, where functional luciferase expression could only be restored if the DNA break was repaired via the non-homologous end joining (NHEJ) repair pathway. A co-transfected plasmid expressing Renilla luciferase served as an internal control for transfection efficiency. Results showed that *PGK1* knockdown significantly increased firefly luciferase activity, confirming enhanced DNA damage repair activity in these cells (Fig. 6F).

Additionally, we observed elevated nuclear levels of 53BP1 in *PGK1* knockdown cells (Fig. 6G). As a key downstream effector of AMPK, 53BP1 is known to promote the NHEJ repair pathway [38], further supporting the role of enhanced DNA damage repair in TMZ resistance.

Taken together, these results indicate that while *PGK1* knockdown does not affect TMZ-induced DNA damage, it significantly enhances DNA damage repair, likely through the AMPK-53BP1 pathway, contributing to TMZ resistance.

***PGK1* expression may serve as a predictive biomarker for TMZ sensitivity in GBM**

Next, we investigated whether *PGK1* expression could serve as a biomarker for TMZ sensitivity. We measured *PGK1* expression levels and assessed TMZ susceptibilities in three additional GBM cell lines: U118 MG, U251 MG, and U251 MG/TMZ (a TMZ-resistant variant of U251 MG) (Fig. 7A). Compared to U251 MG, U118 MG cells exhibited significantly lower *PGK1* expression and

greater TMZ resistance (IC₅₀: 289.7 μ M vs. 54.96 μ M). Similarly, U251 MG/TMZ cells, which are more resistant to TMZ than U251 MG cells (IC₅₀: 99.6 μ M vs. 54.96 μ M), also showed markedly reduced *PGK1* expression levels (Fig. 7B).

To further substantiate these findings, we analyzed clinical data. Specifically, we queried the Cancer Treatment Response gene signature DataBase (CTR-DB) [39, 40], a resource containing patient-derived clinical transcriptomes along with cancer drug response data. Consistent with our observations in cell lines, GBM patients who were non-responsive to TMZ treatment displayed significantly lower *PGK1* expression levels (Fig. 7C).

Additionally, we validated our findings using patient-derived glioma stem cells (GSCs). We have previously generated a GSC cell line (CB5304) from patient-derived GBM tissue (Fig. 7D) [41]. GSCs are widely recognized as a major contributor to therapeutic resistance in GBM. We then tested whether *PGK1* knockdown contributes to TMZ resistance in these patient-derived cells. Using a lentiviral system, we integrated a CRISPR interference (CRISPRi) expression cassette into CB5304 cells. The knockdown efficiency was validated with pre-characterized sgRNAs targeting *STAT1*, *IFNAR1*, and *TRAPPC1* (Supplementary Fig. 2B). Following validation, the CB5304 cells were transduced with either control sgRNAs (sgCtrl) or sgRNAs targeting *PGK1* (sg*PGK1*). Consistent with our previous findings in GBM cell lines, *PGK1* knockdown in patient-derived GSCs significantly enhanced TMZ resistance as measured by the CCK-8 assay (Fig. 7E).

Collectively, these findings across cell lines, patient data, and primary GSCs establish *PGK1* expression as a potential predictive biomarker for TMZ sensitivity in GBM. (Fig. 7F)

Discussion

In this study, we uncovered a paradoxical role of metabolic inhibition in promoting chemoresistance in GBM. Through systematic CRISPRi screens, we identified *PGK1*, a key glycolytic enzyme, as a critical determinant of TMZ sensitivity. While *PGK1* inhibition suppressed tumor growth under normal conditions, it unexpectedly enhanced resistance to TMZ treatment. This finding highlights a previously unappreciated complexity in

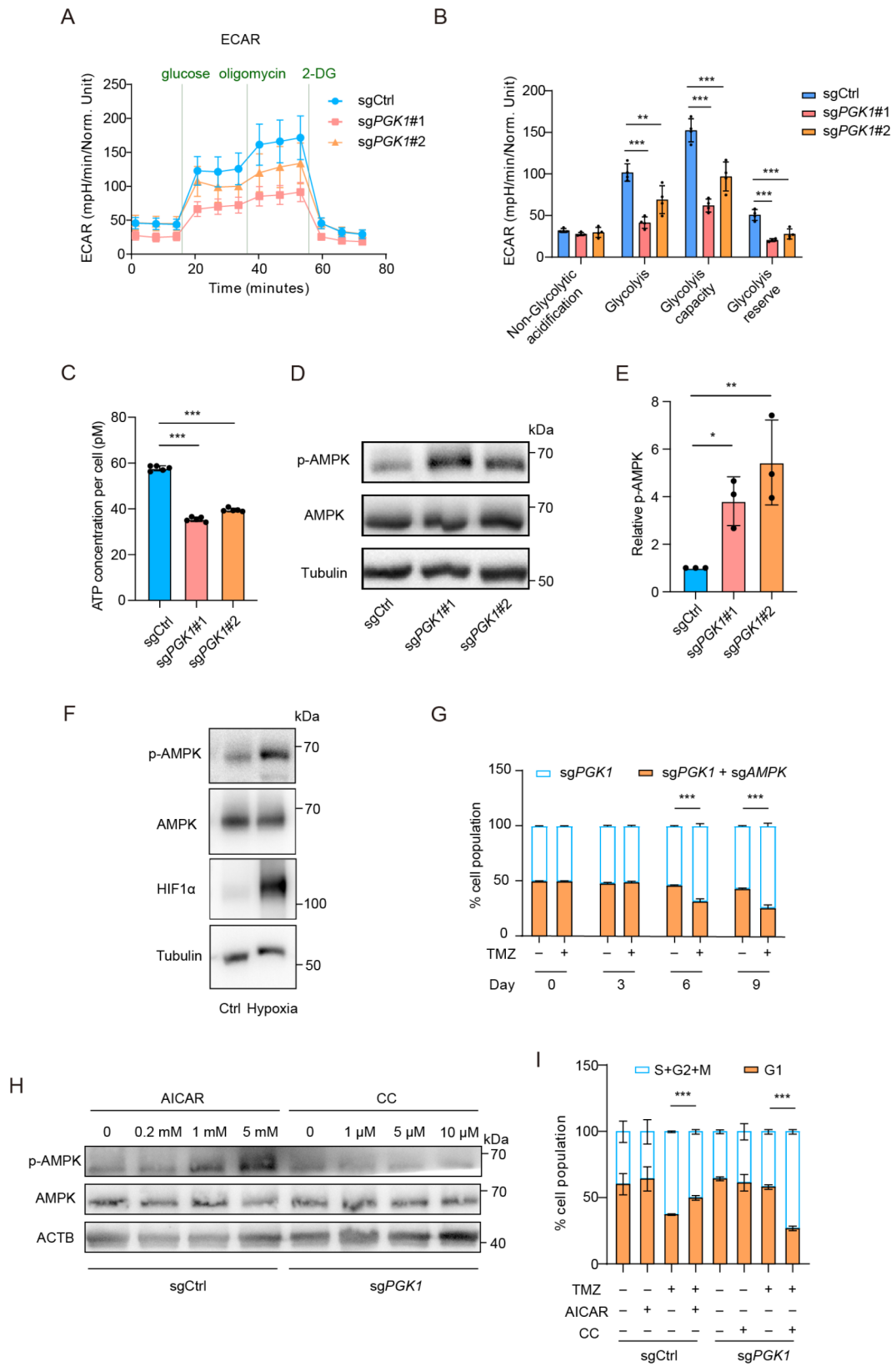


Fig. 5 (See legend on next page.)

(See figure on previous page.)

Fig. 5 AMPK activation mediates TMZ resistance following *PGK1* knockdown. **A, B.** Metabolic characterization by Seahorse assay showing reduced glycolysis, glycolytic capacity and glycolysis reserve in *PGK1* knockdown cells ($n=4$). Error bars denote SD. **C.** Reduced ATP levels in *PGK1* knockdown cells as measured by a bioluminescent assay. Data are presented as mean \pm SD from 3 independent experiments. **D-F.** Western blot analysis of AMPK phosphorylation at T172 in *PGK1* knockdown cells (**D, E**) and under hypoxia (**F**). Data are presented as mean \pm SD from 3 independent experiments. **G.** Competitive growth assay showing reversal of TMZ resistance by AMPK knockdown in *PGK1* knockdown cells. Data are presented as mean \pm SD from 3 independent experiments. **H, I.** Pharmacological activation and inhibition of AMPK by AICAR and Compound C (CC), respectively (**H**), with corresponding cell cycle analysis (**I**). Data are presented as mean \pm SD from 3 independent experiments

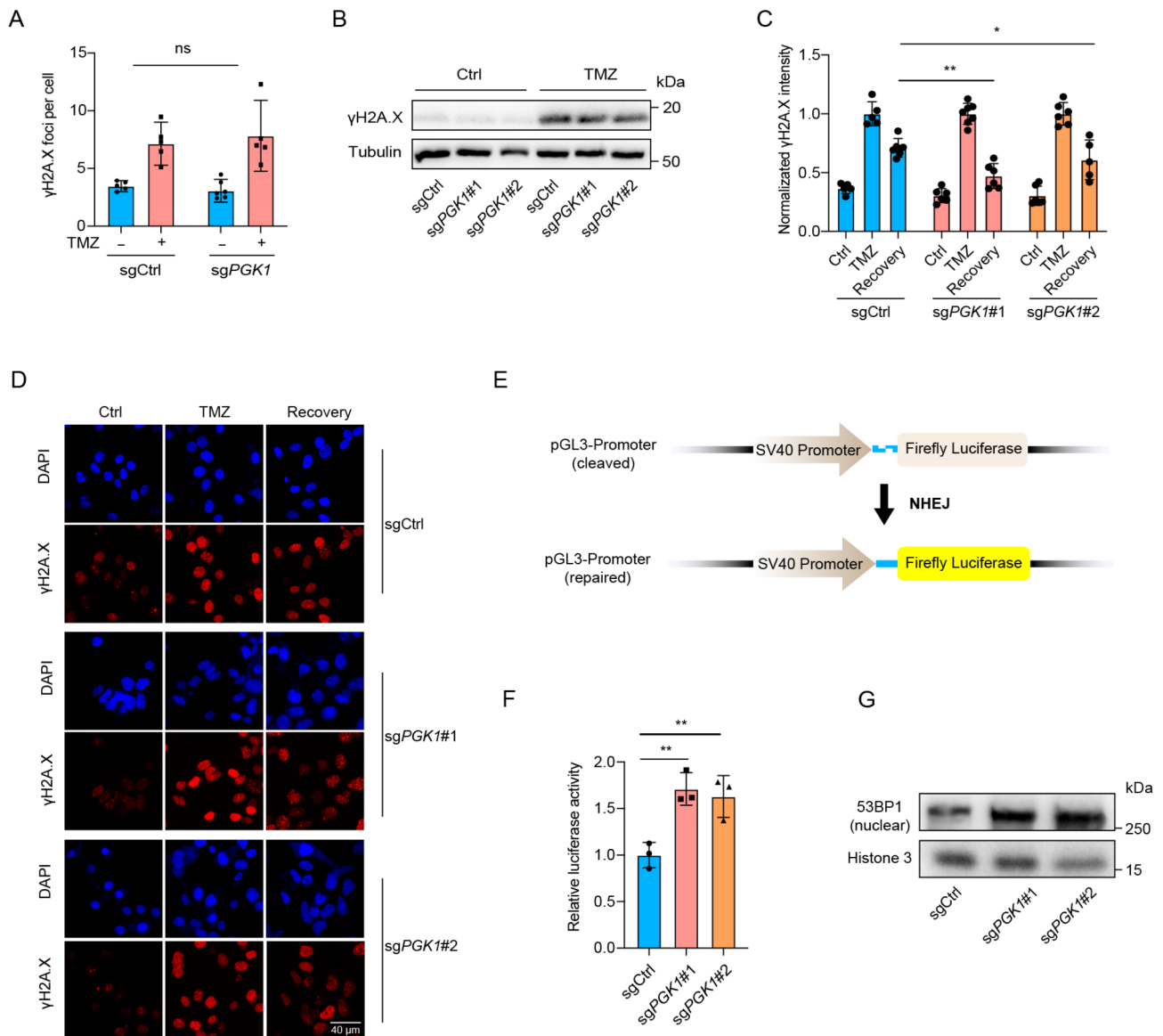


Fig. 6 Enhanced DNA damage repair via AMPK-53BP1 axis in *PGK1* knockdown cells. **A-D.** DNA damage assessment in sgCtrl and sgPGK1 U87 cells. **(A, B)** Immunofluorescence quantification and western blot analysis of γ H2A.X signal following 24 h TMZ (50 μ M) treatment. **(C, D)** Time-course analysis of DNA damage repair showing γ H2A.X levels at 0 h and 24 h after TMZ removal, more than 10 cells of one sample were imaged and counted ($n=5-7$ samples), error bars denote SD. Scale bar, 40 μ m. **E, F.** NHEJ repair capacity assessed using a luciferase-based reporter system. **(E)** Schematic of the dual-luciferase reporter construct containing Hind III-cleaved Firefly luciferase and intact Renilla luciferase. **(F)** Relative repair efficiency quantified by Firefly/Renilla luciferase activity ratio. Data are presented as mean \pm SD from 3 independent experiments. **G.** Western blot analysis and quantification of nuclear 53BP1 protein levels in sgCtrl and sgPGK1 cells

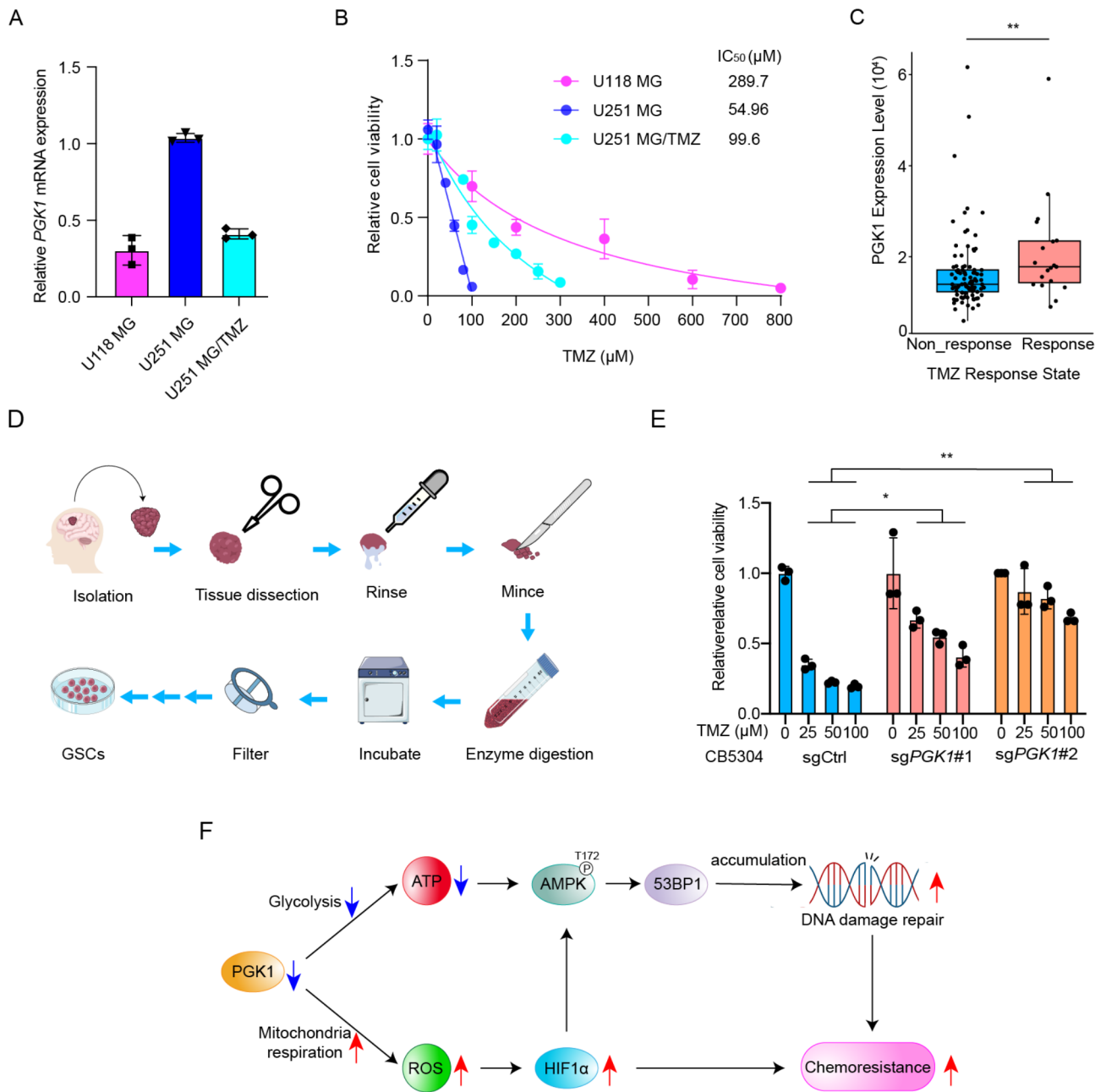


Fig. 7 Clinical Relevance of *PGK1* Expression in TMZ Sensitivity. **A, B.** Comparative analysis of *PGK1* expression and TMZ sensitivity across GBM cell lines. **(A)** *PGK1* expression levels in U118 MG, U251 MG, and TMZ-resistant U251 MG/TMZ cells by qPCR. **(B)** Cell viability assays under TMZ treatment for each cell line. ($n=3$) Error bars denote SD. **C.** Analysis of *PGK1* expression levels in TMZ-responsive versus non-responsive GBM patients from the CTR-DB database ($n=117$ patients). **D, E.** Validation in patient-derived glioma stem cells (GSC line CB5304). **(D)** Procedures of isolating GSCs from patient GBM tissue. **(E)** Effect of *PGK1* knockdown in CB5304 on TMZ sensitivity measured by CCK-8 assay. Data are presented as mean \pm SD from 3 independent experiments. **F.** Proposed mechanistic model of *PGK1* knockdown-induced TMZ resistance in GBM cells. *PGK1* knockdown triggers two parallel pathways promoting TMZ resistance: (1) Reduced glycolytic capacity leads to increased mitochondrial respiration, resulting in elevated ROS levels and subsequent HIF-1 α stabilization. (2) Decreased ATP levels and metabolic stress activate AMPK through phosphorylation at T172. HIF-1 α pathway activation promotes cell survival under stress, while activated AMPK promotes 53BP1 recruitment to DNA damage sites, enhancing DNA damage repair activity. This dual mechanism ultimately confers resistance to TMZ treatment

targeting cancer metabolism: metabolic stress induced by glycolytic inhibition can activate adaptive responses that promote survival under therapeutic pressure.

Mechanistically, we demonstrated that *PGK1* inhibition leads to ATP depletion and subsequent activation of the AMPK pathway, a key cellular energy sensor [42]. Activated AMPK, together with elevated HIF-1 α signaling, enhances DNA damage repair capacity through the 53BP1-dependent pathway, thereby promoting cell survival under TMZ treatment. This mechanism represents a novel link between metabolic stress and DNA damage repair in cancer cells, expanding our understanding of how metabolic perturbations influence therapeutic responses.

Tumor cells adapt their metabolic pathways to generate ATP and supply essential biomacromolecules in response to varying concentrations of external nutrients and stress conditions [43]. Metabolic reprogramming is a critical mechanism enabling tumor cells to adapt to nutrient-deficient and hypoxic environments [44]. This reprogramming profoundly influences the immunosuppressive state of the tumor microenvironment (TME) and tumor progression through several key processes: the accumulation of metabolic products, metabolic adaptation of immune cells such as T cell metabolism and macrophage polarization, and regulation of signaling pathways including PD-1/PD-L1 and PI3K/Akt/mTOR [45, 46].

Our research finding that inhibition of *PGK1* could activate HIF-1 α , leading to enhanced hypoxic responses in GBM cells. HIF-1 α promotes glycolysis and lactate production, which further reinforces the immunosuppressive characteristics of the TME [47]. OXPHOS levels increase following *PGK1* inhibition. The enhancement of OXPHOS has long been recognized to contribute to hypoxia and tumor treatment resistance. This shift can lead to mitochondrial damage and elevated levels of ROS [48]. Consequently, the combination of metabolic stress and the accumulation of depolarized mitochondria synergistically reprograms tumor-infiltrating lymphocytes, resulting in functional impairment and exhaustion [49]. Additionally, hypoxia and metabolic reprogramming synergistically drive chronic inflammation within the TME, thereby facilitating tumor progression [50].

The clinical relevance of our findings is supported by multiple lines of evidence. Analysis of patient-derived GBM samples revealed a strong correlation between *PGK1* expression levels and TMZ sensitivity. This observation was further validated in patient-derived GSCs, suggesting that *PGK1* expression could serve as a predictive biomarker for TMZ response in GBM patients. Moreover, our results in TMZ-resistant cell lines demonstrate that reduced *PGK1* expression is associated with acquired TMZ resistance, indicating that metabolic

adaptation might be a common mechanism underlying treatment resistance in GBM.

These findings have important implications for cancer therapy. First, they caution against the simplistic view of metabolic targeting in cancer treatment, highlighting the need to consider potential adaptive responses that might compromise therapeutic efficacy. Second, they suggest that combining metabolic inhibitors with strategies to block these adaptive responses might be necessary to achieve optimal therapeutic outcomes. For instance, concurrent inhibition of AMPK or DNA damage repair pathways might prevent the development of resistance following metabolic perturbation. Moreover, KEGG enrichment analysis revealed that the PI3K/Akt and NF- κ B signaling pathways are associated with TMZ resistance. Cancer therapies targeting these pathways, such as the use of PI3K or Akt inhibitors in combination with TMZ, can enhance anti-tumor effects. Lastly, for drug resistance, modulating metabolic enzymes may present new therapeutic opportunities.

Several limitations of our study should be noted. While we focused on *PGK1* and glycolysis, other metabolic pathways might also contribute to drug resistance through similar or distinct mechanisms. Additionally, the complex tumor microenvironment in vivo might influence the metabolic dependencies and adaptive responses of GBM cells in ways not captured by our in vitro studies.

Future studies should investigate the broader implications of metabolic stress-induced drug resistance in cancer treatment. This might include comprehensive profiling of metabolic adaptations in resistant tumors, development of strategies to prevent or overcome these adaptive responses, and evaluation of *PGK1* as a predictive biomarker in larger patient cohorts. Understanding these aspects will be crucial for developing more effective therapeutic strategies for GBM and potentially other cancers.

Future perspectives: Integrating single-cell sequencing with metabolomics can provide deeper insights into the intricate interactions between metabolism and immunity within the TME. Individualized treatment strategies: By leveraging patient-specific metabolic and immune profiles, personalized combination therapies can be developed. Exploring novel mechanisms of tumor metabolism and immune evasion will offer new avenues for cancer therapy.

Conclusion

Our study reveals a complex relationship between metabolic perturbation and chemoresistance in GBM.

Through systematic CRISPR screening and mechanistic investigations, our finding mainly revealed that *PGK1* as a critical metabolic node whose inhibition paradoxically promotes TMZ resistance despite suppressing

tumor growth. Inhibiting tumor metabolism may temporarily suppress tumor growth; however, in the long term, it can alter the metabolic pathways of tumors, leading to treatment resistance. This finding highlights the adaptive capacity of cancer cells to leverage metabolic stress for survival advantage under therapeutic pressure.

The elucidation of the *PGK1*-AMPK-53BP1 axis provides mechanistic insight into how metabolic stress can enhance DNA damage repair and promote drug resistance. Furthermore, the consistent correlation between *PGK1* expression and TMZ sensitivity across multiple experimental models and patient samples establishes its potential as a predictive biomarker.

These results have important implications for cancer therapy, particularly cautioning against single-agent metabolic targeting and emphasizing the need for combination strategies that address potential adaptive responses. Future studies should focus on developing therapeutic approaches that can effectively target both metabolic vulnerabilities and resistance mechanisms in GBM.

Abbreviations

AMPK	AMP-activated protein kinase
ATP	Adenosine triphosphate
BFP	Blue fluorescent protein
CCK-8	Cell Counting Kit-8
CRISPRi	CRISPR interference
CTR-DB	Cancer Treatment Response gene signature Database
dCas9	Dead Cas9
DEGs	Differentially expressed genes
DMEM	Dulbecco's Modified Eagle's Medium
GBM	Glioblastoma
GFP	Green fluorescent protein
GSC	Glioma stem cell
HIF-1 α	Hypoxia-inducible factor 1-alpha
IC50	Half-maximal inhibitory concentration
NHEJ	Non-homologous end joining
PGK1	Phosphoglycerate kinase 1
qPCR	Quantitative polymerase chain reaction
ROS	Reactive oxygen species
sgRNA	Single guide RNA
TMZ	Temozolomide

Supplementary Information

The online version contains supplementary material available at <https://doi.org/10.1186/s12967-025-06261-4>.

Additional File 1: Supplementary Figs. 1–3.

Additional File 2: Supplementary Table 1; Results of the U87 growth screen, analyzed by the MAGeCK pipeline.

Additional File 3: Supplementary Table 2; Results of the U87 TMZ resistance screen, analyzed by the MAGeCK pipeline.

Additional File 4: Supplementary Table 3; qPCR primers and sgRNA oligo sequences used in this study.

Additional File 5: Supplementary Table 4; Gene expression levels in FPKM from the RNA-seq analysis.

Acknowledgements

We thank the assistance of SUSTech Core Research Facilities on flow cytometry. We thank Yangyi Zhang from the Hao Chen lab at SUSTech for his

assistance on Seahorse experiments and all members of the Tian lab for the discussion.

Author contributions

RT conceived and supervised the project. XL, WZ, YF and TS designed and conducted experiments with guidance from RT. XL, WZ, YF and RT analyzed data. JC provided the GSC cell line. XL, WZ and RT wrote the manuscript with input from all authors.

Funding

This work was supported by the National Natural Science Foundation of China (32100766 and 82171416 to R.T.), Guangdong Basic and Applied Basic Research Foundation (2023B1515020075 to R.T.), Shenzhen Fundamental Research Program (JCYJ20220530112602006 and RCYX20221008092845052 to R.T.), and Shenzhen Medical Research Fund (A2301054 to Y.F., A2303039 to R.T.).

Data availability

All data generated or analyzed during this study are included in this article.

Declarations

Ethics approval and consent to participate

Not applicable to this study.

Consent for publication

All authors have read and approved the publication of the manuscript.

Competing interests

The authors have declared that no competing interest exists.

Received: 17 December 2024 / Accepted: 14 February 2025

Published online: 06 March 2025

References

1. Tan AC, Ashley DM, López GY, Malinzak M, Friedman HS, Khasraw M. Management of glioblastoma: state of the Art and future directions. *CA Cancer J Clin.* 2020;70(4):299–312.
2. De Silva MI, Stringer BW, Bardy C. Neuronal and tumourigenic boundaries of glioblastoma plasticity. *Trends Cancer.* 2023;9(3):223–36.
3. Ostrom QT, Price M, Neff C, Cioffi G, Waite KA, Kruchko C, et al. CBTRUS statistical report: primary brain and other central nervous system tumors diagnosed in the united States in 2016–2020. *Neuro Oncol.* 2023;25(12 Suppl 2):iv1–99.
4. Tomar MS, Kumar A, Srivastava C, Shrivastava A. Elucidating the mechanisms of Temozolomide resistance in gliomas and the strategies to overcome the resistance. *Biochim Biophys Acta Rev Cancer.* 2021;1876(2):188616.
5. Stupp R, Hegi ME, Mason WP, van den Bent MJ, Taphoorn MJ, Janzer RC, et al. Effects of radiotherapy with concomitant and adjuvant Temozolomide versus radiotherapy alone on survival in glioblastoma in a randomised phase III study: 5-year analysis of the EORTC-NCIC trial. *Lancet Oncol.* 2009;10(5):459–66.
6. Hegi ME, Dierens AC, Gorlia T, Hamou MF, de Tribolet N, Weller M, et al. MGMT gene Silencing and benefit from Temozolomide in glioblastoma. *N Engl J Med.* 2005;352(10):997–1003.
7. Lunt SY, Vander Heiden MG. Aerobic glycolysis: meeting the metabolic requirements of cell proliferation. *Annu Rev Cell Dev Biol.* 2011;27:441–64.
8. Wong KKL, Verheyen EM. Metabolic reprogramming in cancer: mechanistic insights from *Drosophila*. *Dis Model Mech.* 2021;14(7):1–17.
9. Tufail M, Jiang CH, Li N. Altered metabolism in cancer: insights into energy pathways and therapeutic targets. *Mol Cancer.* 2024;23(1):203.
10. Yang J, Shay C, Saba NF, Teng Y. Cancer metabolism and carcinogenesis. *Exp Hematol Oncol.* 2024;13(1):10.
11. Ganapathy-Kanniappan S, Geschwind JF. Tumor Glycolysis as a target for cancer therapy: progress and prospects. *Mol Cancer.* 2013;12:152.
12. Galluzzi L, Kepp O, Heiden MG, Kroemer G. Metabolic targets for cancer therapy. *Nat Rev Drug Discovery.* 2013;12(11):829–46.
13. Rajabi L, Ebrahimdoost M, Mohammadi SA, Soleimani Samarkhazan H, Khamisipour G, Aghaei M. Aqueous and ethanolic extracts of *Moringa*

- oleifera leaves induce selective cytotoxicity in Raji and Jurkat cell lines by activating the P21 pathway independent of P53. *Mol Biol Rep.* 2025;52(1):102.
14. Gonçalves AC, Richiardon E, Jorge J, Polónia B, Xavier CPR, Salaroglio IC, et al. Impact of cancer metabolism on therapy resistance - Clinical implications. *Drug Resist Updat.* 2021;59:100797.
 15. Demicco M, Liu X-Z, Leithner K, Fendt S-M. Metabolic heterogeneity in cancer. *Nat Metabolism.* 2024;6(1):18–38.
 16. Fendt SM, Frezza C, Erez A. Targeting metabolic plasticity and flexibility dynamics for Cancer therapy. *Cancer Discov.* 2020;10(12):1797–807.
 17. Lee CJ, Yoon H. Metabolic adaptation and cellular stress response as targets for Cancer therapy. *World J Mens Health.* 2024;42(1):62–70.
 18. Tian R, Gachechiladze MA, Ludwig CH, Laurie MT, Hong JY, Nathaniel D, et al. CRISPR Interference-Based platform for multimodal genetic screens in human iPSC-Derived neurons. *Neuron.* 2019;104(2):239–55.e12.
 19. Tian R, Abarientos A, Hong J, Hashemi SH, Yan R, Dräger N, et al. Genome-wide CRISPRi/a screens in human neurons link lysosomal failure to ferroptosis. *Nat Neurosci.* 2021;24(7):1020–34.
 20. Samelson AJ, Tran QD, Robinot R, Carrau L, Rezelj VV, Kain AM, et al. BRD2 Inhibition blocks SARS-CoV-2 infection by reducing transcription of the host cell receptor ACE2. *Nat Cell Biol.* 2022;24(1):24–34.
 21. Horlbeck MA, Gilbert LA, Villalta JE, Adamson B, Pak RA, Chen Y et al. Compact and highly active next-generation libraries for CRISPR-mediated gene repression and activation. *Elife.* 2016;5.
 22. Li X, Sun S, Zhang W, Liang Z, Fang Y, Sun T, et al. Identification of genetic modifiers enhancing B7-H3-targeting CART cell therapy against glioblastoma through large-scale CRISPRi screening. *J Exp Clin Cancer Res.* 2024;43(1):95.
 23. Xu D, Shao F, Bian X, Meng Y, Liang T, Lu Z. The evolving landscape of non-canonical functions of metabolic enzymes in Cancer and other pathologies. *Cell Metab.* 2021;33(1):33–50.
 24. Li X, Jiang Y, Meisenhelder J, Yang W, Hawke DH, Zheng Y, et al. Mitochondria-Translocated PGK1 functions as a protein kinase to coordinate Glycolysis and the TCA cycle in tumorigenesis. *Mol Cell.* 2016;61(5):705–19.
 25. Nie H, Ju H, Fan J, Shi X, Cheng Y, Cang X, et al. O-GlcNAcylation of PGK1 coordinates Glycolysis and TCA cycle to promote tumor growth. *Nat Commun.* 2020;11(1):36.
 26. Ababneh O, Nishizaki D, Kato S, Kurzrock R. Tumor necrosis factor superfamily signaling: life and death in cancer. *Cancer Metastasis Rev.* 2024;43(4):1137–63.
 27. Alim LF, Keane C, Souza-Fonseca-Guimaraes F. Molecular mechanisms of tumour necrosis factor signalling via TNF receptor 1 and TNF receptor 2 in the tumour microenvironment. *Curr Opin Immunol.* 2024;86:102409.
 28. Taniguchi K, Karin M. NF- κ B, inflammation, immunity and cancer: coming of age. *Nat Rev Immunol.* 2018;18(5):309–24.
 29. He Y, Sun MM, Zhang GG, Yang J, Chen KS, Xu WW, et al. Targeting PI3K/Akt signal transduction for cancer therapy. *Signal Transduct Target Ther.* 2021;6(1):425.
 30. Shvetsova AN, Mennerich D, Kerätär JM, Hiltunen JK, Kietzmann T. Non-electron transfer chain mitochondrial defects differently regulate HIF-1 α degradation and transcription. *Redox Biol.* 2017;12:1052–61.
 31. Lacher SE, Levings DC, Freeman S, Slattery M. Identification of a functional antioxidant response element at the HIF1A locus. *Redox Biol.* 2018;19:401–11.
 32. Akter R, Awais M, Boopathi V, Ahn JC, Yang DC, Kang SC, et al. Inversion of the Warburg effect: unraveling the metabolic Nexus between obesity and Cancer. *ACS Pharmacol Transl Sci.* 2024;7(3):560–69.
 33. Steinberg GR, Hardie DG. New insights into activation and function of the AMPK. *Nat Rev Mol Cell Biol.* 2023;24(4):255–72.
 34. Sharma A, Anand SK, Singh N, Dwivedi UN, Kakkar P. AMP-activated protein kinase: an energy sensor and survival mechanism in the reinstatement of metabolic homeostasis. *Exp Cell Res.* 2023;428(1):113614.
 35. Qian X, Li X, Tan L, Lee JH, Xia Y, Cai Q, et al. Conversion of PRPS hexamer to monomer by AMPK-Mediated phosphorylation inhibits nucleotide synthesis in response to energy stress. *Cancer Discov.* 2018;8(1):94–107.
 36. Rothbart SB, Racanelli AC, Moran RG. Pemetrexed indirectly activates the metabolic kinase AMPK in human carcinomas. *Cancer Res.* 2010;70(24):10299–309.
 37. Jiang Y, Cong X, Jiang S, Dong Y, Zhao L, Zang Y, et al. Phosphoproteomics reveals the AMPK substrate network in response to DNA damage and histone acetylation. *Genomics Proteom Bioinf.* 2022;20(4):597–613.
 38. Jiang Y, Dong Y, Luo Y, Jiang S, Meng FL, Tan M, et al. AMPK-mediated phosphorylation on 53BP1 promotes c-NHEJ. *Cell Rep.* 2021;34(7):108713.
 39. Jiang J, Ma Y, Yang L, Ma S, Yu Z, Ren X et al. CTR-DB 2.0: an updated cancer clinical transcriptome resource, expanding primary drug resistance and newly adding acquired resistance datasets and enhancing the discovery and validation of predictive biomarkers. *Nucleic Acids Res.* 2024.
 40. Liu Z, Liu J, Liu X, Wang X, Xie Q, Zhang X, et al. CTR-DB, an omnibus for patient-derived gene expression signatures correlated with cancer drug response. *Nucleic Acids Res.* 2022;50(D1):D1184–99.
 41. Wu M, Wang T, Ji N, Lu T, Yuan R, Wu L, et al. Multi-omics and Pharmacological characterization of patient-derived glioma cell lines. *Nat Commun.* 2024;15(1):6740.
 42. Sadria M, Seo D, Layton AT. The mixed blessing of AMPK signaling in Cancer treatments. *BMC Cancer.* 2022;22(1):105.
 43. Xia L, Oyang L, Lin J, Tan S, Han Y, Wu N, et al. The cancer metabolic reprogramming and immune response. *Mol Cancer.* 2021;20(1):28.
 44. Nong S, Han X, Xiang Y, Qian Y, Wei Y, Zhang T et al. Metabolic reprogramming in cancer: Mechanisms and therapeutics. *MedComm (2020).* 2023;4(2):e218.
 45. Kao KC, Vilbois S, Tsai CH, Ho PC. Metabolic communication in the tumour-immune microenvironment. *Nat Cell Biol.* 2022;24(11):1574–83.
 46. Aghapour SA, Torabizadeh M, Bahreiny SS, Saki N, Jalali Far MA, Yousefi-Avarvand A, et al. Investigating the dynamic interplay between cellular immunity and tumor cells in the fight against cancer: an updated comprehensive review. *Iran J Blood Cancer.* 2024;16(2):84–101.
 47. Shen H, Ojo OA, Ding H, Mullen LJ, Xing C, Hossain MI, et al. HIF1 α -regulated Glycolysis promotes activation-induced cell death and IFN- γ induction in hypoxic T cells. *Nat Commun.* 2024;15(1):9394.
 48. Beerkens APM, Heskamp S, Reinema FV, Adema GJ, Span PN, Bussink J. Mitochondria-targeting of oxidative phosphorylation inhibitors to alleviate hypoxia and enhance anticancer treatment efficacy. *Clin Cancer Res.* 2025.
 49. Yu YR, Imrichova H, Wang H, Chao T, Xiao Z, Gao M, et al. Disturbed mitochondrial dynamics in CD8(+) TILs reinforce T cell exhaustion. *Nat Immunol.* 2020;21(12):1540–51.
 50. Shao C, Yang F, Miao S, Liu W, Wang C, Shu Y, et al. Role of hypoxia-induced exosomes in tumor biology. *Mol Cancer.* 2018;17(1):120.

Publisher's note

Springer Nature remains neutral with regard to jurisdictional claims in published maps and institutional affiliations.